

Erica Stevens

Department of Mechanical Engineering and
Materials Science,
University of Pittsburgh,
Pittsburgh, PA 15261
e-mail: ericastevens@pitt.edu

Katerina Kimes

Department of Mechanical Engineering and
Materials Science,
University of Pittsburgh,
Pittsburgh, PA 15261
e-mail: kak272@pitt.edu

Volodymyr Chernenko

BCMaterials & University of the Basque Country
(UPV/EHU), Campus of Leioa,
Leioa 48940, Spain;
Ikerbasque, Basque Foundation for Science,
Bilbao 48013, Spain
e-mail: volodymyr.chernenko@ehu.eus

Patricia Lázpita

BCMaterials & University of the Basque Country
(UPV/EHU), Campus of Leioa,
Leioa 48940, Spain
e-mail: patricia.lazpita@ehu.eus

Anna Wojcik

Institute of Metallurgy and Materials Science,
Polish Academy of Sciences,
25 Reymonta Street,
30-059 Cracow, Poland
e-mail: anna2307.wojcik@gmail.com

Wojciech Maziarz

Institute of Metallurgy and Materials Science,
Polish Academy of Sciences,
25 Reymonta Street,
30-059 Cracow, Poland
e-mail: w.maziarz@imim.pl

Jakub Toman

Department of Mechanical Engineering and
Materials Science,
University of Pittsburgh,
Pittsburgh, PA 15261
e-mail: jakub.toman@pitt.edu

Markus Chmielus¹

Department of Mechanical Engineering and
Materials Science,
University of Pittsburgh,
Pittsburgh, PA 15261
e-mail: chmielus@pitt.edu

Effect of Homogenization on the Microstructure and Magnetic Properties of Direct Laser-Deposited Magnetocaloric $\text{Ni}_{43}\text{Co}_7\text{Mn}_{39}\text{Sn}_{11}$

Transitioning current cooling and refrigeration technologies to solid-state cooling leveraging the magnetocaloric effect would improve efficiency and eliminate a harmful influence on the environment. Employing additive manufacturing as a production method would increase geometrical freedom and allow designed channels and porosity in heat exchangers made from magnetocaloric materials, to increase surface area for heat transfer via a fluid. This study is the first to demonstrate a successful deposition of the $\text{Ni}_{43}\text{Co}_7\text{Mn}_{39}\text{Sn}_{11}$ magnetocaloric material by direct laser deposition. Samples were defined as either properly- or overbuilt, and representative ones were characterized for microstructural features before and after homogenization heat treatment, as well as magnetic behavior and constituent phases. As-built microstructures consisted of dendrites, columnar grains, and elongated cells, with a mix of both austenite and 7M martensite phases. Homogenization increased the fraction of 7M martensite, and encouraged distinct equiaxed and columnar grains, eliminating dendrites and cellular structures. The increased fraction of the weak magnetic martensitic phase also resulted in a strong reduction of the saturation magnetization. Some differences in structure and performance may be related to an energy density difference causing higher Mn loss in the properly built sample, with a lower powder-to-energy input ratio. As a whole, it is found that direct laser deposition (DLD) additive manufacturing of Ni-Mn-based magnetocaloric material is very promising, since representative transformation, phase state, and magnetic properties have been achieved in this study. [DOI: 10.1115/1.4046900]

Keywords: $\text{Ni}_{43}\text{Co}_7\text{Mn}_{39}\text{Sn}_{11}$ magnetic shape memory alloy, additive manufacturing, X-ray micro-computed tomography, martensitic transformation, twinning, directed energy deposition, additive manufacturing, advanced materials and processing, laser processes

1 Introduction

Cooling in the household and industry consumes a significant portion of the world-wide electricity; therefore, refrigeration technologies are constantly under improvement [1]. Until recently, all

room-temperature cooling was performed using the vapor-compression cycle which requires a vacuum environment for the coolant, potentially harmful chemicals as coolants, and a noisy compressor. Magnetic refrigeration leverages the magnetocaloric effect (MCE) to generate solid-state cooling that is more efficient in the refrigeration cycle and does not require a vacuum environment, harmful chemicals, or noisy compressors. Materials that exhibit MCE show a temperature change when exposed to a magnetic field under adiabatic conditions (ΔT_{ad}) [2]. According to

¹Corresponding author.

Manuscript received July 31, 2019; final manuscript received April 2, 2020; published online April 14, 2020. Assoc. Editor: Steven Schmid.

theoretical calculations, these multifunctional materials could increase the efficiency of the room-temperature refrigeration technology by up to 30% and replace liquid-gas with solid-state cooling [3–5].

The materials that experience a large temperature change upon adiabatic (de-)magnetization resulting from the magnetic field-induced first-order phase transformations exhibit a so-called giant conventional or inverse MCE [6,7]. Particularly, the Heusler-type Ni-Mn-X (X = In, Sn, and Sb) metamagnetic shape memory alloys, exhibiting martensitic transformation (MT) from the ferromagnetic austenite into weakly magnetic martensite, show a giant inverse MCE, meaning that they cool upon adiabatic magnetization [8–11]. A simple refrigeration cycle using an inverse MCE material is illustrated and explained in Fig. 1. These Ni-Mn-based alloys are relevant because they can produce a large ΔT_{ad} near room temperature, do not require rare earth metals, and their MT properties can be easily tuned by doping.

As already mentioned, the inverse MCE arises due to the existence of a sharp increase in magnetization upon MT into the austenitic phase, causing absorption of thermal energy. In Ni-Mn-X (X = In, Sn, Sb), the application of a magnetic field shifts the MT temperature [10,12], allowing the tetragonal or orthorhombic martensite (recognized by a banded surface structure called twinning) to be transformed into cubic austenite [13]. The higher the difference between the magnetization of austenite and martensite, the more sensitive MT is to the applied magnetic field [14].

Currently, magnetocaloric materials are produced by a number of different methods. La-Fe-Si-based alloys have been fabricated by arc and induction melting, though a subsequent week-long homogenization was required to eliminate coarse dendrites [15]. In order to avoid long homogenization times, rapid solidification methods of melt spinning and strip casting became common [16–19]. Ribbons and flakes created from melt spinning or strip casting can be ground into powder for use in powder metallurgy methods, a processing route that has been examined for La-Fe-Si, Mn-P-based, and Ni-Mn-(Sn, In) Heusler alloys [20–24]. Though there has been only one prior report of laser-based additive

manufactured (AM) for magnetocaloric materials, selective laser melting of LaFe_{11.7}Co_{1.3}Si [25], combining the spatial freedom of AM with the functionality of magnetocaloric materials would greatly increase their potential applications by enabling an increase in surface area through the creation of designed porosity or channels needed for the flowing heat transfer fluid [4,26]. There are several of our previous works regarding the additive manufacturing (both laser-based and powder bed binder jet 3D printing) of Ni-Mn-based functional magnetic alloys [23,27–30]. In addition, Laitinen et al. have also recently published works on the laser powder bed fusion of Ni-Mn-Ga magnetic shape memory alloys [31,32].

Direct laser deposition (DLD) is a type of directed energy deposition AM where metal powder is sprayed through nozzles in the direction of a melt pool created by a laser. Some of the powder adds to the melt pool volume, and the laser and powder nozzles move as a unit relative to the part in a pre-determined path with each layer. This is in contrast with laser powder bed methods of AM where a laser selectively melts powder that is already deposited into a bed. Thus, with some attention to the laser power and powder flow parameters [33], the workpiece in DLD is built up to the desired specifications in three dimensions with very little powder waste and low powder volume requirements. This process is most well-known for the selective repair of parts but can also be used for fabrication [34,35]. AM is a desirable method for the fabrication of limited numbers of items and complicated geometries due to the time and cost-savings over traditional manufacturing.

This study aims to demonstrate the potential of functional DLD AM for the magnetocaloric Ni-Co-Mn-Sn by microstructural, phase transformation, and magnetic property evaluation. After powder characterization by optical microscopy (OM), scanning electron microscopy (SEM), and X-ray micro-computed tomography (μ CT), the printed workpiece was assessed through an investigation of the presence and distribution of twinning using OM and SEM. MT was identified using differential scanning calorimetry (DSC). The magnetic properties were assessed by using vibrating sample magnetometry (VSM), and structure was analyzed using X-ray diffraction (XRD).

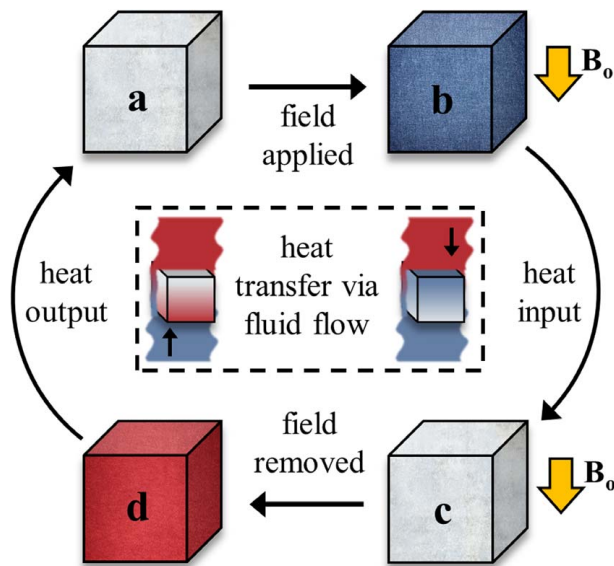


Fig. 1 Cooling cycle for a material exhibiting the inverse magnetocaloric effect. (a→b) The material begins at a nominal temperature. When a magnetic field is applied, the material spontaneously cools down. (b→c) Heat to be removed from an external source such as a refrigerator is transferred to the material via fluid flow. (c→d) The magnetic field is removed, and the material spontaneously heats up. (d→a) Excess heat is removed from the material via fluid flow, returning the system to its original state.

2 Experimental

Ni₄₃Co₇Mn₃₉Sn₁₁ powder was produced by melt spinning and mechanical grinding. A small amount of powder was cold mounted and polished to a final step of colloidal silica for characterization. As-received powder morphology was qualified for mounted and unmounted samples (to capture both projected size and cross-sectional size) with Keyence VHX-600 OM and Zeiss Sigma 500 SEM imaging. Powder size distribution was quantified using OM and SEM images analyzed using IMAGEJ software [36], as well as with a Bruker SkyScan1272 μ CT. A total of 35 particle images obtained with OM and SEM from both mounted and unmounted powders were analyzed using IMAGEJ software. Due to resolution limitations, only particles greater than 5 μ m in equivalent diameter were included in the analysis. The μ CT imaging of powders was performed at 100 kV and 100 μ A and with 0.11-mm Cu filter, with a pixel size of 2 μ m and a rotation step of 0.1 deg. Powders were compacted into an X-ray translucent straw wrapped in Parafilm, and random movement was turned off during scanning in order to reduce particle shifting. All subsequent reconstruction, analysis, and visualization were carried out using Micro Photonics-provided Bruker software (NRecon, Dataviewer, CTAn, CTVOx). The particle size was measured using 3D volume analysis to calculate equivalent diameter (using only values $\geq 5 \mu$ m for consistency and resolution limits).

Samples of five layers (two neighboring parallel lines per layer) were deposited onto a nickel substrate (2 × 2 × 0.25 in., 99.99% Ni) using an Optomec LENS 450 system. The Optomec LENS 450 system was equipped with a 1070-nm continuous wave Ytterbium fiber laser that had a spot diameter of 570 μ m at standard deposition nozzle stand-off height. Shielding gas used was industrial-purity Ar,

Table 1 Printing parameters for exemplary properly built (PB) and overbuilt (OB) samples. The powder mass flowrate measurement is described in the experimental section.

Sample	Laser power (W)	Layer height (mm)	Powder feed rate (rpm)	Powder mass flowrate (g/min)	Hatch spacing (mm)
PB	200	0.25	5	2.0	0.25
OB	200	0.51	6	2.5	0.51

flowing over the melt pool. Parameter optimization and powder flow testing were not performed because of the limited amount of available powder. Two types of samples were identified during printing: properly built (PB) and overbuilt (OB). Deposition parameter changes were not the sole cause of sample type changes; samples with the same deposition parameters had the potential to be PB or OB samples. Varied machine parameters are listed in Table 1 for a PB and OB exemplary sample, each of which was chosen after initial characterization of seven printed samples. Note that rotations per minute (rpm) is given as the unit of measure for powder flow since this is the most replicable value given the inconsistent powder mass flowrate. However, an average flowrate is also given from collection experiments lasting 30 s for each bag collected. With a very limited amount of powder, four bags of powder were collected at steady-state conditions for 5 rpm (range of 0.4 g/min), but a similar ball-milled powder was used to collect at both 5 rpm (two samples, range of 0.2 g/min) and 6 rpm (three samples, range of 1.0 g/min), confirming that the same average value was obtained for 5 rpm. During deposition, nozzle travel speed was held constant at 2.5 mm/s. Our study is focused on microstructures present in these two build types (PB and OB), without assuming any correlation to build parameters, since irregular powder particles can also cause inconsistent powder flow.

All samples were cut in half parallel to the laser scanning direction with a wire saw. One half was mounted and polished in the same manner as the powder, and the other was retained in the as-printed state. Mounted samples were examined with the Zeiss Sigma 500, equipped with energy-dispersive X-ray spectroscopy (EDS) for elemental analysis. Unmounted samples were characterized for magnetic and thermal properties in the as-printed state and then encapsulated in an argon-purged vacuum atmosphere with a titanium sponge oxygen-getter and heat-treated for homogenization at 1000 °C for 4 h, with a ramp of 10 °C/min and air cooling. These samples were then mounted, polished, and again unmounted. The final surface finish for SEM imaging was achieved with an SEM ion mill. Homogenized samples will be referred to as PB_{hom} and OB_{hom}.

Non-homogenized and homogenized sample halves were used for DSC, VSM, and XRD measurements. Thermal properties were measured with a DSC from 0 to 300 °C, though only relevant ranges will be plotted for clarity. Magnetic property measurements were taken with a Lakeshore 7407 VSM from -2 to 2 T with a ramp cycle of 0 T → 2 T → -2 T → 2 T. Testing with a Cu-K α source Bruker D8 Discover XRD was performed in the range of 20 deg \leq $2\theta \leq$ 94 deg with an increment of 0.02 deg, scan speed 1 s/step, and slit size 0.6 mm. XRD pattern analysis was conducted using the FULLPROF software [37].

3 Results and Discussion

3.1 Powder. Powder characterization was performed with OM, SEM, and μ CT. Morphological observations showed that the particle shapes are irregular (as defined by the standard of powder metallurgy ASTM B243-13), as expected for the pulverized powder of brittle material.

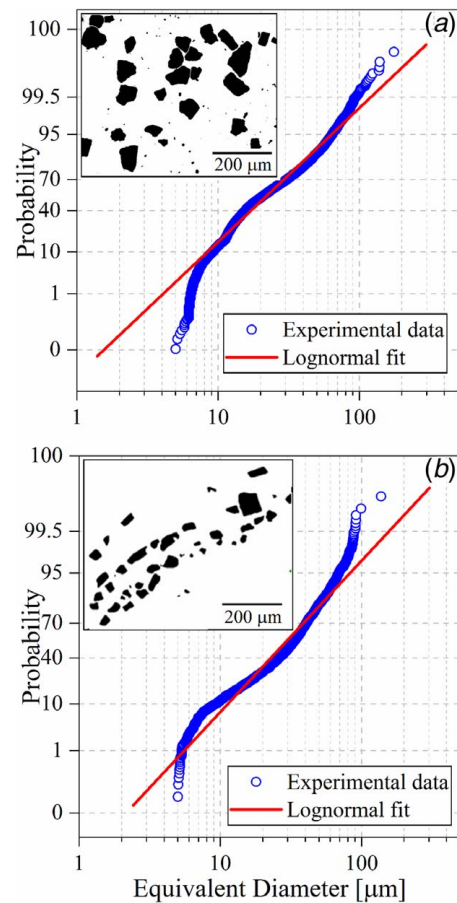


Fig. 2 Powder size distribution compared to a lognormal fit. (a) Data collected using optical and electron microscopy. (b) Data collected using X-ray μ CT. Insets are exemplary binarized images from each technique, showing powder shape and size in projection for (a) and in a 2D slice for (b).

In view of the probability plots shown in Fig. 2, the particles approximately followed a lognormal distribution, with the circle-equivalent diameters from 5–176 μ m, where the lower limit of 5 μ m reflected resolution limits and the upper end of particle sizes had a positive deviation away from the lognormal line. IMAGEJ analysis of OM and SEM images took into account the full range of 5–176 μ m equivalent diameters, and the data were plotted in Fig. 2(a). Morphology and size distribution were also evaluated using μ CT, with similar results. A 3D visualization with μ CT confirmed that the powder was mostly granular (approximately equidimensional, non-spherical). The equivalent diameter calculated from the 3D volume data yielded the results shown in Fig. 2(b). After conglomerated particles were removed, the sphere-equivalent diameters ranged 5–138 μ m. The recommended spherical particle range for DLD is 44–150 μ m [38,39].

3.2 Structure and Composition. Two types of samples were observed after deposition: properly built (PB) and overbuilt (OB), and one example of each was chosen for comparison of the microstructure produced in this material after laser melting and homogenization. Figure 3 shows the lengthwise cross-sectional views of the PB and OB samples, with the layer boundaries shown as dotted gray lines. As detailed in Table 2 and indicated with gray and white area fill in Fig. 3, there are two distinct sections of the samples. In both samples, there is a bottom section that has relatively even layer boundary spacing, and melt pool boundaries are also in consistent intervals. Nearer to the top, however, the layer boundaries become far apart or inconsistently placed. Hereafter, the sections

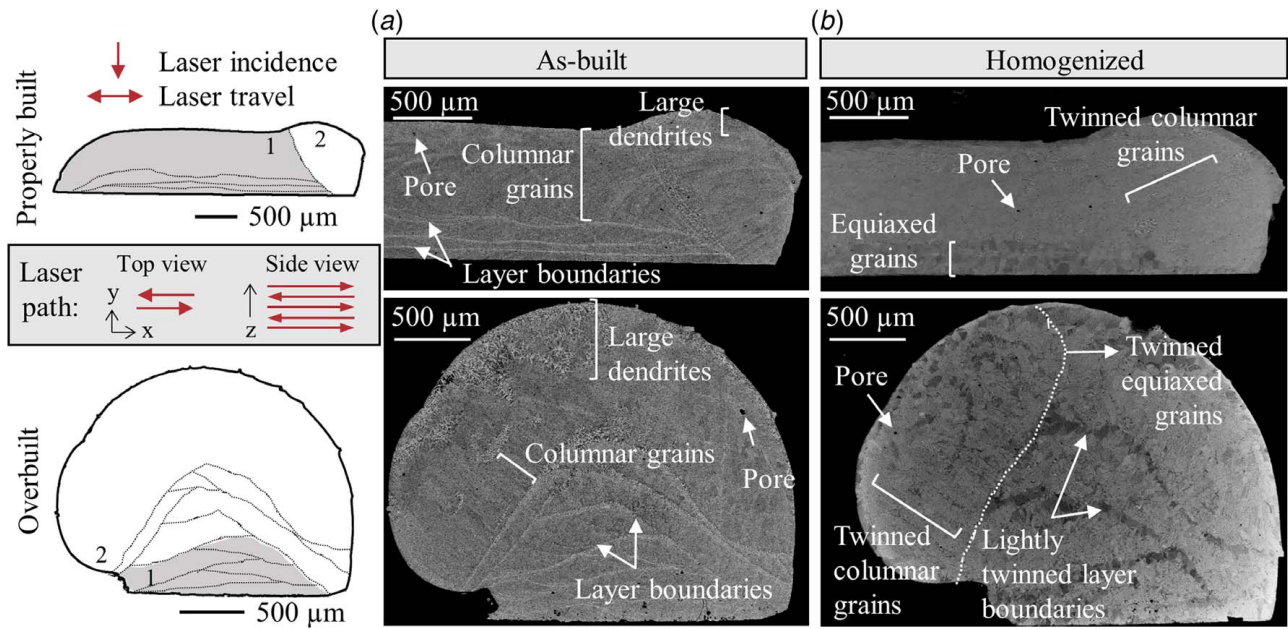


Fig. 3 (a) PB and OB sample schematics showing the PB-1, PB-2, OB-1, and OB-2 sections of the samples as well as the visible boundaries between printed layers. (b) Right panels showing as-built and homogenized sample micrographs are marked with the prevalent regions of microstructural features before and after homogenization. Laser travel, incidence, and path are also indicated.

Table 2 Feature descriptions of sections within the PB and OB samples

Section	Melt pools	Layers	Microstructural features
1	Consistent spacing	Thin and consistent height	Fine, elongated cells
2	Inconsistent spacing	Thicker and inconsistent spacing	Dendrites, columnar grains, and elemental microsegregation

will be referred to by the sample name and section name (PB-1, PB-2, OB-1, and OB-2).

Figure 3 also shows an overview of the microstructural features observed through backscatter electron images in both the as-built and homogenized samples. Both the PB-1 and OB-1 as-printed sections had a relatively fine microstructure of elongated cells, with a transition to columnar grains and then relatively large (tens of micrometers long) dendrites by the top of both PB-2 and OB-2. Magnified views of these microstructural features are shown in Fig. 4.

After homogenization, layer boundaries were blurred in both samples as shown in Figs. 4(e)–4(h). Equiaxed grains developed

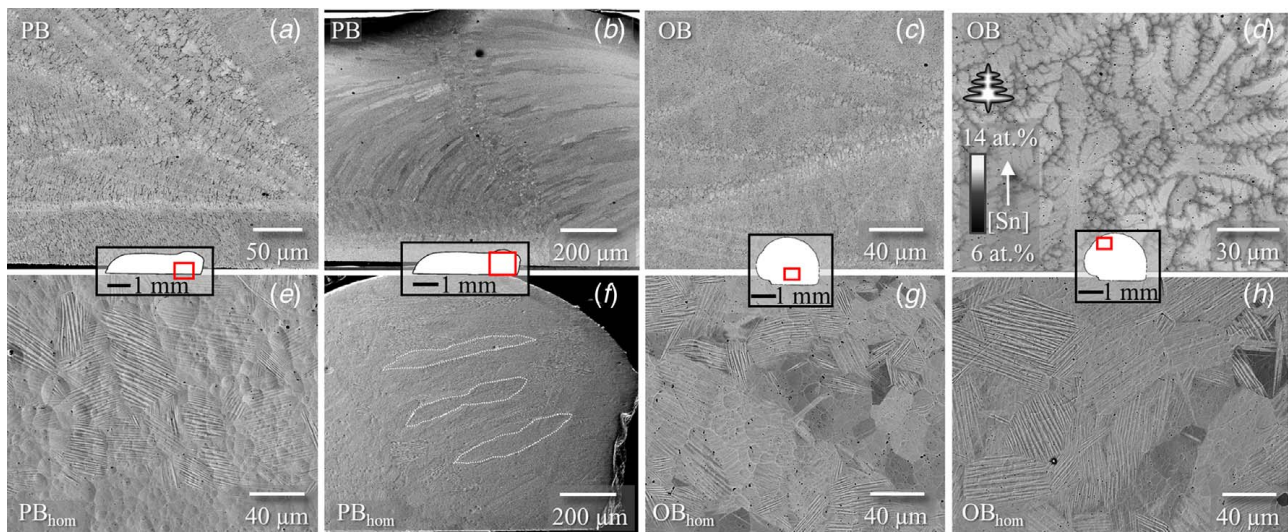


Fig. 4 Examples of microstructural features throughout (a–d) as-built and (e–h) homogenized samples and the level of Sn microsegregation within the dendritic region of (d) as-built OB. Insets indicate the region from which the as-built/homogenized micrograph pair was obtained. White dotted areas in (f) trace columnar grains. Crater-like artifacts are a result of ion milling as a final preparation step and have no effect on grains or twin structures.

Table 3 EDS composition data averaged over sample matrix in the as-built and homogenized state, all with ± 1.0 at% uncertainty, together with corresponding electronic concentration, e/a . OB as-built data are from a comparable sample

at%	Ni	Mn	Co	Sn	e/a
PB	44.5	36.4	6.6	12.5	8.09
PB _{hom}	46.0	36.6	7.4	10.0	8.23
OB	43.0	37.8	6.5	12.7	8.04
OB _{hom}	45.2	36.8	7.5	10.5	8.19
Nominal	43.0	39.0	7.0	11.0	8.10

in the bottom PB-1 and OB-1 sections, as well as some toward the top sections (Figs. 4(e), 4(g), and 4(h)). Columnar grains remained unchanged after homogenization (Fig. 4(f)), and twinning was—in contrast to as-deposited samples—ubiquitous, implying a uniform or nearly uniform presence of the martensite phase, indicating a well-homogenized sample.

Composition determined by EDS varied from the nominal Ni₄₃Co₇Mn₃₉Sn₁₁, particularly in the dendritic region shown in Fig. 4. Interdendritic regions were approximately Ni₄₃Co₁₂Mn₃₉Sn₆ average from all samples, and matrix (excluding interdendritic regions) compositions for each sample are given in Table 3 and compared with homogenized composition data. Ni concentration increased in the as-built matrix from the nominal and increased further after homogenization. From the nominal composition, there was a decrease in Mn by 2–3 at% in the as-built sample matrix, which was not recovered after homogenization. There was also a slight decrease in Co in the as-built sample matrix, but this was recovered and surpassed the nominal composition of 7 at% in

Table 4 Phase and lattice parameters determined using XRD patterns

Sample	Phase	a (Å)	b (Å)	c (Å)	β (deg)
PB	L2 ₁ (Fm $\bar{3}$ m)	5.98			
	Monoclinic 7M	4.30	5.36	29.22	93.50
PB _{hom}	L2 ₁ (Fm $\bar{3}$ m)	5.97			
	Monoclinic 7M	4.32	5.38	29.31	94.47
OB	Disordered (Pm3m)	5.96			
	Monoclinic 7M	4.29	5.34	29.11	94.37
OB _{hom}	L2 ₁ (Fm $\bar{3}$ m)	5.96			
	Monoclinic 7M	4.31	5.38	29.31	94.49

the homogenized samples. Conversely, there was an increase in Sn in the as-built matrix, which dissipated and reached a level ~ 1 at% lower than nominal after homogenization.

With compositions so varied, XRD was necessary to determine the phases present; all patterns are shown in Fig. 5. The XRD patterns for the as-printed OB sample were indexed as a mixture between a cubic disordered structure (Pm3m space group) and a low symmetry 7M monoclinic martensitic phase, with homogenization leading to the appearance of an L2₁ ordered Fm $\bar{3}$ m phase (Table 4). Similarly, the PB sample began in the as-printed condition with a 7M martensitic phase, but was progressively replaced by the ordered cubic L2₁ phase, which remained after homogenization. For the PB sample, there was also an unidentified peak near 39 deg that was reduced by heat treatment.

In as-deposited samples, EDS analysis showed that sub-grain boundaries (interdendritic regions) were significantly depleted in Sn, while dendrite cores (composition given in Table 3) were slightly Sn-enriched. Sn segregation is a well-known occurrence

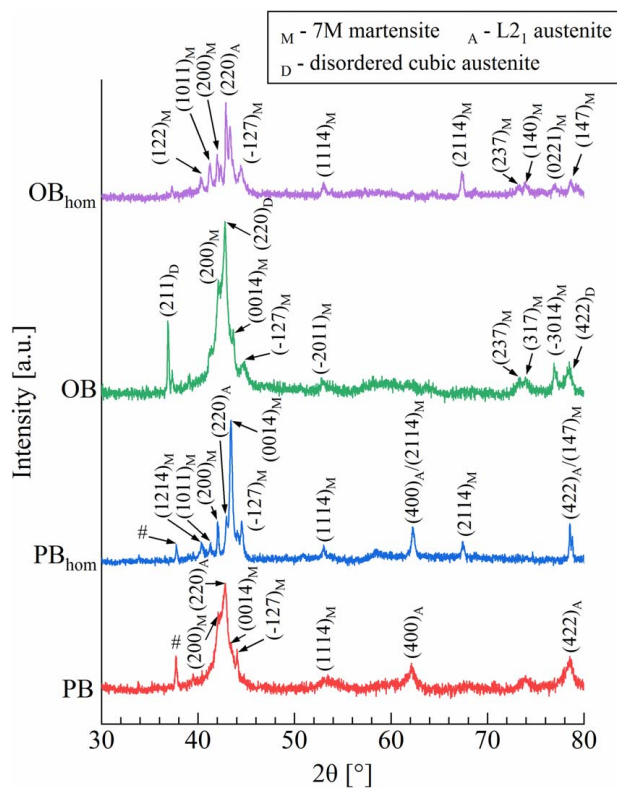


Fig. 5 (A) Room-temperature XRD patterns showing L2₁ austenitic and (D) disordered cubic austenitic, and martensitic (M) peaks and their indices. The # symbol marks an unidentified peak that does not correspond to the austenitic, martensitic, or face-centered cubic (FCC)- γ phases

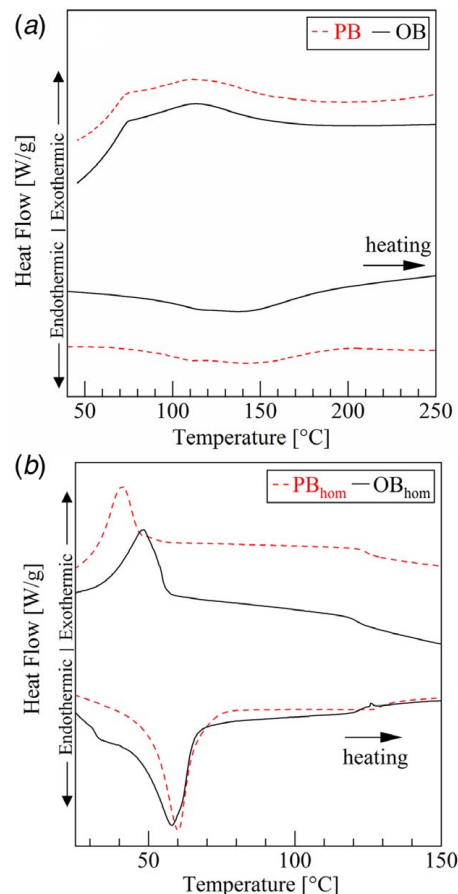


Fig. 6 DSC curves for (a) as-built and (b) homogenized samples

Table 5 Transformation temperatures (M_s , M_f , T_M , A_s , A_f , T_A , and T_C) and room-temperature magnetization values at 2 T applied magnetic field for homogenized samples. \pm values represent uncertainty related to the tangent method measurement of the transformation temperatures.

	M_s (°C)	M_f (°C)	T_M (°C)	A_s (°C)	A_f (°C)	T_A (°C)	T_C (°C)	M_{2T} (Am ² /kg)
PB _{hom}	47 ± 1	32 ± 1	39.5 ± 2	52 ± 1	67 ± 1	59.5 ± 2	125 ± 3	14.7
OB _{hom}	57 ± 1	36 ± 1	46.5 ± 2	49 ± 1	66 ± 1	57.5 ± 2	121 ± 1	19.4

in casting of other alloys such as Cu-Ni-Sn due to the low melting point of Sn [40]; thus, it is not unexpected that fast and repeated thermal fluctuations experienced by the material in DLD also produce Sn segregation [41]. Twinning presence varied throughout the segregated regions, indicating a difference in the phases present. This is supported by DSC data in Fig. 6(a), where the transformation peaks are significantly broadened. The broad peak is a combination of many small peaks at slightly different peak locations that correspond to the different compositions present on the micro-scale within these samples. Indeed, even small compositional changes are known to have a large effect on the MT temperature of Ni-Mn-based functional magnetic materials [42,43]. After homogenization however, this microsegregation was mitigated, as evidenced by the much narrower transformation peaks seen in Fig. 6(b) and by EDS data.

Composition compared between the nominal, as-built matrix, and homogenized states shows how the elements are lost and redistributed within the material. From the nominal composition of Ni₄₃Co₇Mn₃₉Sn₁₁, there was a loss of Mn in the as-built state that was not recovered in the homogenized state. Since Mn has a low vapor pressure, it has been shown that a small amount is lost during full melting with the laser during the deposition process [31,32]. There is slightly greater loss of Mn in the PB sample, which may be due to the increased energy density present in the process. Although the laser power and scan speed were held constant, there would have been a higher energy density in the smaller sample (PB) because there was less influx of material.

XRD patterns show that the as-built samples did contain 7M martensite, and either an ordered or disordered cubic phase. The reduction of the (220)_A peak intensity of the austenitic phase indicates that the heat treatment promotes the growth of the martensitic phase. Moreover, the sharp drop of the (211)_B peak intensity in the OB sample can be associated with an atomic rearrangement of the cubic phase (cubic disordered to L2₁ ordered). The PB sample contained L2₁ rather than the cubic disordered phase, which is likely a result of the differences in composition and composition distribution between the OB and PB samples. The PB sample also showed an

unidentified peak that did not match with the cubic disordered, L2₁, or 7M phases, and also did not correspond to the FCC- γ phase that has been seen for this composition type [44–46].

3.3 Martensitic Transformation. As-built samples showed very broad transformation peaks on DSC curves, plotted in Fig. 6(a). Though distinct MT temperatures are difficult to extract, the reverse martensitic transformation (martensite to austenite) occurred over a range of approximately 90–170 °C and the forward transformation (austenite to martensite) occurred over a range of 60–140 °C. Both the PB and OB as-built DSC curves have the same shape and do not show a distinct Curie temperature (T_C).

After homogenization (Fig. 6(b)), as expected with the elimination of microsegregation, the MT peaks were more distinct, and the range of transformation decreased significantly. Using the tangent method, martensite and austenite start and finish transformation temperatures (M_s , M_f , A_s , and A_f) were determined and are shown in Table 5, along with $T_M = (M_s + M_f)/2$ and $T_A = (A_s + A_f)/2$. T_C was very close in both samples.

Cong et al. reported the austenitic peak of induction melted and annealed Ni₄₃Co₇Mn₃₉Sn₁₁ to be \sim 57 °C and the martensitic peak to be \sim 34 °C [47]. Observed here for PB_{hom} and OB_{hom} were $T_A = 59.5$ °C and 57.5 °C; $T_M = 39.5$ °C and 46.5 °C. Though the austenitic peak data tends to agree, the martensitic peak for the current samples is 5.5–12.5 °C higher. This discrepancy is attributed to slight differences in composition of the samples from the nominal, giving rise to a difference in e/a from the nominal 8.10–8.23 in PB_{hom} and 8.19 in OB_{hom}, respectively. Due to similar reasons, there is also a 7 °C increase in T_M from the PB_{hom} to OB_{hom} sample.

3.4 Magnetization Behavior. Figure 7 shows the room-temperature magnetization curves for each sample and for their homogenized counterparts. At 2 T, PB and OB samples reached 47.8 A·m²/kg and 43.9 A·m²/kg, respectively. Homogenized PB and OB samples at 2 T reached 14.7 and 19.4 A·m²/kg, respectively. Heat treatment therefore led to a drop of 33.1 A·m²/kg (69.2%) in PB and 24.5 A·m²/kg (55.8%) in OB. This drop in magnetization is due to the increase in the volume fraction of martensitic phase within the samples, since the weakly magnetic martensite phase does not react as strongly to an applied field as the ferromagnetic austenite phase does [14].

4 Summary and Conclusions

In this first study of DLD additive manufactured magnetocaloric material, we have demonstrated that deposition was successful and resulted in structurally intact samples. The structural and functional differences between an overbuilt and properly built part, both as-built and homogenized have been examined. Particularly, prior to homogenization, as-built sample structure showed dendrites, columnar grains in the overbuilt area, elongated cells in the properly built area, and a mix of cubic austenite and 7M martensite. After homogenization, sample structure showed equiaxed grains in the properly built area, persisting columnar grains in the overbuilt area, and a decrease in the austenite fraction in favor of the 7M martensitic phase. The latter effect was explained by some loss of Mn.

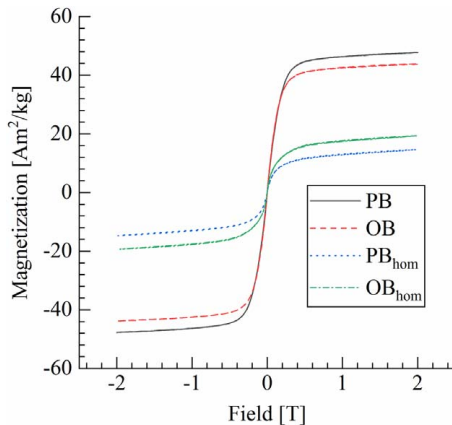


Fig. 7 M-H plot showing a drop in magnetization from the as-built to the homogenized samples measured at room temperature

The characteristics of the martensitic transformation and magnetism of the additive manufactured Ni-Mn-Co-Sn samples have been tuned to be comparable with those observed in the similar MCE alloy produced by conventional methods.

Thus, we have shown that DLD additive manufacturing processing of Ni-Mn-based MCE materials is a very promising technology, as it has demonstrated an effective reproduction of typical MCE materials transformation and magnetic properties in the present work. If direct laser deposition is pursued as a fabrication method, powder flow control would need to be addressed to correct the inconsistent overbuilding. It is likely that using spherical powder of 44–150 μm , as recommended for DLD, would improve the consistency of the powder flowrate. Further progress is therefore expected after the preparation of spherical MCE material powder with a plasma atomization process. Other future work includes using an additive manufacturing technique with a wider range of acceptable powder morphologies (non-powder feeder, powder bed methods).

Acknowledgment

Authors acknowledge funding from the University of Pittsburgh Mascaro Center for Sustainable Innovation. The financial support of the Spanish Ministry of Science, Innovation, and Universities (MICIU) (Project No. RTI2018-094683-B-C53), the Basque Government under the ELKARTEK program (Project No. KK-2018/00099), the Basque Government Department of Education (Project No. IT1245-19), and the Polish National Science Centre (Project no. DEC-2012/06/M/ST8/00451) are greatly acknowledged. This project was also supported in part by a fellowship award through the National Defense Science and Engineering Graduate (NDSEG) Fellowship Program, sponsored by the Air Force Research Laboratory (AFRL), the Office of Naval Research (ONR), and the Army Research Office (ARO). K. Kimes was partially supported by the Swanson School of Engineering at the University of Pittsburgh. J. Toman was partially supported through NSF (Grant No. 1808082). Characterization work was performed at the University of Pittsburgh at the Peterson Institute of Nanoscience and Engineering Nanoscale Fabrication and Characterization Facility (PINSE NCF), the Materials Micro-Characterization Laboratory (MMCL), and the Materials Characterization Lab (MCL).

References

- [1] IEA, 2017, "World Energy Outlook 2017," Int. Energy Agency.
- [2] Weiss, P., and Piccard, A., 1917, "Le Phénomène Magnéto-calorique," *J. Phys. Theor. Appl.*, **7**(1), pp. 103–109.
- [3] Pecharsky, V. K., and Gschneidner, K. A., 1999, "Magnetocaloric Effect and Magnetic Refrigeration," *J. Magn. Magn. Mater.*, **200**(1–3), pp. 44–56.
- [4] Fähler, S., and Pecharsky, V. K., 2018, "Caloric Effects in Ferroic Materials," *MRS Bull.*, **43**(4), pp. 264–268.
- [5] Lyubina, J., 2017, "Magnetocaloric Materials for Energy Efficient Cooling," *J. Phys. D: Appl. Phys.*, **50**(5), p. 053002.
- [6] Franco, V., Blázquez, J. S., Ipus, J. J., Law, J. Y., Moreno-Ramírez, L. M., and Conde, A., 2018, "Magnetocaloric Effect: From Materials Research to Refrigeration Devices," *Prog. Mater. Sci.*, **93**, pp. 112–232.
- [7] Pecharsky, V. K., Gschneidner, K. A., Pecharsky, A. O., and Tishin, A. M., 2001, "Thermodynamics of the Magnetocaloric Effect," *Phys. Rev. B: Condens. Matter Mater. Phys.*, **64**(14), pp. 1444061–14440613.
- [8] Mañosa, L., Moya, X., Planes, A., Krenke, T., Acet, M., and Wassermann, E. F., 2008, "Ni-Mn-based Magnetic Shape Memory Alloys: Magnetic Properties and Martensitic Transition," *Mater. Sci. Eng., A*, **481–482**(1–2C), pp. 49–56.
- [9] Krenke, T., Duman, E., Acet, M., Moya, X., Mañosa, L., and Planes, A., 2007, "Effect of Co and Fe on the Inverse Magnetocaloric Properties of Ni-Mn-Sn," *J. Appl. Phys.*, **102**(3), pp. 1–6.
- [10] Barandiarán, J. M., Chernenko, V. A., Cesari, E., Salas, D., Lazpita, P., Gutierrez, J., and Orue, I., 2013, "Magnetic Influence on the Martensitic Transformation Entropy in Ni-Mn-In Metamagnetic Alloy," *Appl. Phys. Lett.*, **102**(7), pp. 1–5.
- [11] Chernenko, V. A., L'vov, V. A., Cesari, E., and Barandiarán, J. M., 2019, *Fundamentals of Magnetocaloric Effect in Magnetic Shape Memory Alloys*, 1st ed., Elsevier B.V., pp. 1–45.
- [12] Moya, X., Mañosa, L., Planes, A., Aksoy, S., Acet, M., Wassermann, E. F., and Krenke, T., 2008, "Effect of External Fields on the Martensitic Transformation in Ni-Mn Based Heusler Alloys," *Adv. Mater. Res.*, **52**, pp. 189–197.
- [13] Dubenko, I., Samanta, T., Kumar Pathak, A., Kazakov, A., Prudnikov, V., Stadler, S., Granovsky, A., Zhukov, A., and Ali, N., 2012, "Magnetocaloric Effect and Multifunctional Properties of Ni-Mn-Based Heusler Alloys," *J. Magn. Magn. Mater.*, **324**(21), pp. 3530–3534.
- [14] Lázpita, P., Barandiarán, J. M., Chernenko, V. A., Valle García, B., Díaz Tajada, E., Lograsso, T., and Schlagel, D. L., 2014, "Magnetic Properties of Ni_{40+x}Mn_{39-x}Sn₂₁ (x=0, 2, 4, 6 and 8at%) Heusler Alloys," *J. Alloys Compd.*, **594**, pp. 171–174.
- [15] Bruno, N. M., Huang, Y. J., Dennis, C. L., Li, J. G., Shull, R. D., Ross, J. H., Chumlyakov, Y. I., and Karaman, I., 2016, "Effect of Grain Constraint on the Field Requirements for Magnetocaloric Effect in Ni₄₅Co₅Mn₄₀Sn₁₀melt-Spun Ribbons," *J. Appl. Phys.*, **120**(7), pp. 075101.
- [16] Sánchez Llamazares, J. L., Ibarra-Gaytán, P., Sánchez-Valdés, C. F., Álvarez-Alonso, P., and Martínez-Iniesta, A. D., 2017, "Synthesis and Magnetocaloric Characterization of Rapidly Solidified ErMn₂melt-Spun Ribbons," *Intermetallics*, **88**, pp. 41–45.
- [17] Sánchez Llamazares, J. L., Ibarra-Gaytán, P., Sánchez-Valdés, C. F., Álvarez-Alonso, P., and Varga, R., 2019, "Enhanced Magnetocaloric Effect in Rapidly Solidified HoNi₂melt-Spun Ribbons," *J. Alloys Compd.*, **774**, pp. 700–705.
- [18] Alev, A. M., Batdalov, A. B., Kamilov, I. K., Koledov, V. V., Shavrov, V. G., Buchelnikov, V. D., García, J., Prida, V. M., and Hernando, B., 2010, "Magnetocaloric Effect in Ribbon Samples of Heusler Alloys Ni-Mn-M (M = In, Sn)," *Appl. Phys. Lett.*, **97**(21), pp. 35–38.
- [19] Zou, N., Li, Z., Zhang, Y., Sánchez-Valdés, C. F., Sánchez Llamazares, J. L., Esling, C., Yang, B., Zhao, X., and Zuo, L., "Transformation Process Dependent Magnetocaloric Properties of Annealed Ni₅₀Mn₁₈Cu₇Ga₂₅Ribbons," *J. Alloys Compd.*, **698**, pp. 731–738.
- [20] Katter, M., Zellmann, V., Reppel, G. W., and Uestuener, K., 2008, "Magnetocaloric Properties of La(Fe, Co, Si) 13 Bulk Material Prepared by Powder Metallurgy," *IEEE Trans. Magn.*, **44**(11 PART 2), pp. 3044–3047.
- [21] Zhong, X. C., Feng, X. L., Huang, X. W., Shen, X. Y., and Liu, Z. W., 2016, "Structure and Magnetocaloric Effect of La_{0.7}Ce_{0.3}(Fe_{0.92}Co_{0.08})_{11.4}Si_{1.6}bulk Alloy Prepared by Powder Metallurgy," *J. Alloys Compd.*, **685**, pp. 913–916.
- [22] Lozano, J. A., Kostow, M. P., Bru, E., De Lima, J. C., Prata, A. T., and Wendhausen, P. A. P., 2008, "Porous Manganese-Based Magnetocaloric Material for Magnetic Refrigeration at Room Temperature," *J. Magn. Magn. Mater.*, **320**(14), pp. 189–192.
- [23] Stevens, E., Kimes, K., Chernenko, V., Lazpita, P., Wojcik, A., Maziarz, W., and Chmielus, M., 2018, "Direct Laser Deposition and Homogenization of Ni-Co-Mn-Sn Magnetocaloric Materials," *Microsc. Microanal.*, **24**(S1), pp. 956–957.
- [24] Maziarz, W., Wojcik, A., Czaja, P., Zywczak, A., Dutkiewicz, J., Hawelek, Ł., and Cesari, E., 2016, "Magneto-Structural Transformations in Ni₅₀Mn_{37.5}Sn_{12.5}-XInx Heusler Powders," *J. Magn. Magn. Mater.*, **412**, pp. 123–131.
- [25] Moore, J. D., Klemm, D., Lindackers, D., Grasemann, S., Träger, R., and Eckert, J., 2013, "Selective Laser Melting of La (Fe, Co, Si) 13 Geometries for Magnetic Refrigeration," *J. Appl. Phys.*, **114**(4), pp. 1–9.
- [26] Fähler, S., Röbler, U. K., Kastner, O., Eckert, J., Eggeler, G., Emmerich, H., Entel, P., Müller, S., Quandt, E., and Albe, K., "Caloric Effects in Ferroic Materials: New Concepts for Cooling," *Adv. Eng. Mater.*, **14**(1–2), pp. 10–19.
- [27] Mostafaei, A., Kimes, K. A., Stevens, E. L., Toman, J., Krimer, Y. L., Ullakko, K., and Chmielus, M., 2017, "Microstructural Evolution and Magnetic Properties of Binder jet Additive Manufactured Ni-Mn-Ga Magnetic Shape Memory Alloy Foam," *Acta Mater.*, **131**, pp. 482–490.
- [28] Toman, J., Müllner, P., and Chmielus, M., 2018, "Properties of As-Deposited and Heat-Treated Ni-Mn-Ga Magnetic Shape Memory Alloy Processed by Directed Energy Deposition," *J. Alloys Compd.*, **752**, pp. 455–463.
- [29] Stevens, E., Kimes, K., Chernenko, V., Wojcik, A., Maziarz, W., Toman, J., and Chmielus, M., 2017, "Characterization of Direct Laser Deposited Magnetocaloric Ni-Co-Mn-Sn," *Materials Science and Technology 2017*, Pittsburgh, PA, Oct. 8–12.
- [30] Stevens, E., Toman, J., Kimes, K., Chernenko, V., Wojcik, A., and Chmielus, M., 2016, "Microstructural Evaluation of Magnetocaloric Ni-Co-Mn-Sn Produced by Directed Energy Deposition," *Microscopy Microanal.*, **22**(Suppl 3), pp. 1774–1775.
- [31] Laitinen, V., Salminen, A., and Ullakko, K., 2019, "First Investigation on Processing Parameters for Laser Powder Bed Fusion of Ni-Mn-Ga Magnetic Shape Memory Alloy," *J. Laser Appl.*, **31**(2), p. 022303.
- [32] Laitinen, V., Sozinov, A., Saren, A., Salminen, A., and Ullakko, K., 2019, "Laser Powder bed Fusion of Ni-Mn-Ga Magnetic Shape Memory Alloy," *Addit. Manuf.*, **30**, p. 100891.
- [33] Katinas, C., Liu, S., and Shin, Y. C., 2019, "Self-sufficient Modeling of Single Track Deposition of Ti-6Al-4V With the Prediction of Capture Efficiency," *ASME J. Manuf. Sci. Eng.*, **141**(1), pp. 1–10.
- [34] Pranievicz, M., Kurfess, T., and Saldana, C., 2019, "An Adaptive Geometry Transformation and Repair Method for Hybrid Manufacturing," *ASME J. Manuf. Sci. Eng.*, **141**(1), pp. 1–8.
- [35] Bennett, J., Garcia, D., Kendrick, M., Hartman, T., Hyatt, G., Ehmman, K., You, F., and Cao, J., 2019, "Repairing Automotive Dies With Directed Energy Deposition: Industrial Application and Life Cycle Analysis," *ASME J. Manuf. Sci. Eng.*, **141**(2), pp. 1–9.
- [36] Schneider, C. A., Rasband, W. S., and Eliceiri, K. W., 2012, "NIH Image to ImageJ: 25 Years of Image Analysis," *Nat. Methods*, **9**(7), pp. 671–675.
- [37] Rodríguez-Carvajal, J., 1993, "Recent Advances in Magnetic Structure Determination by Neutron Powder Diffraction," *Phys. B*, **192**(1–2), pp. 55–69.

- [38] Gu, D. D., Meiners, W., Wissenbach, K., and Poprawe, R., 2012, "Laser Additive Manufacturing of Metallic Components: Materials, Processes and Mechanisms," *Int. Mater. Rev.*, **57**(3), pp. 133–164.
- [39] Kakinuma, Y., Mori, M., Oda, Y., Mori, T., Kashihara, M., Hansel, A., and Fujishima, M., 2016, "Influence of Metal Powder Characteristics on Product Quality With Directed Energy Deposition of Inconel 625," *CIRP Ann.—Manuf. Technol.*, **65**(1), pp. 209–212.
- [40] Guo, Z., Jie, J., Liu, S., Liu, J., Yue, S., Zhang, Y., and Li, T., 2020, "Solidification Characteristics and Segregation Behavior of Cu-15Ni-8Sn Alloy," *Metall. Mater. Trans. A Phys. Metall. Mater. Sci.*, **51**(3), pp. 1229–1241.
- [41] Li, J., Wang, Q., and Michaleris, P., 2018, "An Analytical Computation of Temperature Field Evolved in Directed Energy Deposition," *ASME J. Manuf. Sci. Eng.*, **140**(10), p. 101004.
- [42] Graf, T., Felser, C., and Parkin, S. S. P., 2011, "Simple Rules for the Understanding of Heusler Compounds," *Prog. Solid State Chem.*, **39**(1), pp. 1–50.
- [43] Entel, P., Buchelnikov, V. D., Khovailo, V. V., Zayak, A. T., Adeagbo, W. A., Gruner, M. E., Herper, H. C., and Wassermann, E. F., 2006, "Modelling the Phase Diagram of Magnetic Shape Memory Heusler Alloys," *J. Phys. D: Appl. Phys.*, **39**(5), pp. 865–889.
- [44] Pérez-Sierra, A. M., Pons, J., Santamarta, R., Vermaut, P., and Ochín, P., 2015, "Solidification Process and Effect of Thermal Treatments on Ni–Co–Mn–Sn Metamagnetic Shape Memory Alloys," *Acta Mater.*, **93**, pp. 164–174.
- [45] Lázpita, P., Sasmaz, M., Cesari, E., Barandiarán, J. M., Gutiérrez, J., and Chernenko, V. A., 2016, "Martensitic Transformation and Magnetic Field Induced Effects in Ni₄₂Co₈Mn₃₉Sn₁₁ Metamagnetic Shape Memory Alloy," *Acta Mater.*, **109**, pp. 170–176.
- [46] Chen, F., Tong, Y. X., Huang, Y. J., Tian, B., Li, L., and Zheng, Y. F., 2013, "Suppression of γ Phase in Ni 38 Co 12 Mn 41 Sn 9 Alloy by Melt Spinning and Its Effect on Martensitic Transformation and Magnetic Properties," *Intermetallics*, **36**, pp. 81–85.
- [47] Cong, D. Y., Roth, S., and Schultz, L., 2012, "Magnetic Properties and Structural Transformations in Ni-Co-Mn-Sn Multifunctional Alloys," *Acta Mater.*, **60**(13–14), pp. 5335–5351.